University of Zurich

Tuning the Critical Field of the Bose-Einstein Condensation in $Ba_{3-x}Sr_xCr_2O_8$

Philippe Hasler

Bachelor's Thesis

Group: Prof. Dr. A. Schilling
Supervisors: Henrik Grundmann and Fabian von Rohr

September 11, 2014

Abstract

In this Bachelor's thesis the critical magnetic fields of the Bose-Einstein condensed (BEC) phase in the quantum spin-dimer system $Ba_{3-x}Sr_xCr_2O_8$ is investigated. This work aims to contribute to the remaining question of the influence of different x values on the critical magnetic field. In the first part, the magnetization M as a function of the temperature T of the polycrystalline samples is measured using the superconducting quantum interference device (SQUID) of the Physics Department of the University of Zurich. As the second part, the magnetization M as a function of the magnetic field H is measured in high-field magnetometry experiments. These measurements are performed at the High Magnetic Field Laboratory in Dresden-Rossendorf (HZDR).

Table of Contents

1 Basic Principles

1.1 Bose-Einstein Condensation (BEC)

In 1925 A. Einstein [2] predicted a phenomenom where identical bosonic particles or molecules of an ideal gas occupy the lowest quantum state if the system is sufficiently cooled [5]. Einstein's work based on the ideas of S. N. Bose [3] who derived the Planck law for black-body radiation by treating the photons as a gas of identical bosonic particles.

Cooling a system of bosons to temperatures close to absolute zero allows most of the bosons to occupy the ground state simultaneously. This is only possible for bosons since they have integer spin and do not obey the Pauli principle (in contrast to fermions). Furthermore, these „condensed" particles are not separated in real space from the non-condensed particles but in momentum space [4]. The behaviour of the system can then be described by a single macroscopic wave function. One has to emphasize that the condensation is only driven by the particle statistics and not by their interactions.

Today this phenomenon is called „Bose-Einstein condensation" (BEC). The first experimental evidence for this specific phase transition could finally be obtained in superfluid ^{4}He and later on in dilute atomic gases by groups at the JILA and the MIT in 1995 [1].

As recent research [7, 10, 12, 13, 14] has indicated, the concept of BEC is not only applicable for cold gases or liquid helium but also for bosonic quasiparticles in solids.

1.2 BEC of triplons in spin-dimer systems

In order to describe the reduction of spontaneous magnetization by thermal fluctuations in solids F. Bloch [6] introduced the concept of magnons in 1930. Magnons are particles with integer spin and therefore obey Bose-Einstein statistics. Furthermore they can be seen as quantized spin waves (analogous to phonons in crystal lattices) [8].
In addition to Blochs work, Matsubara and Matsuda used a lattice model to describe the peculiar properties of liquid helium in 1956 [9]. They were able to show that there exists an exact correspondence between a magnet and a lattice Bose gas.
These investigations led to the question whether it is possible for magnons to undergo a BEC. In 2000, researchers at the Tokyo Institute of Technology were able to answer this question by interpreting magnetization data as a BEC of magnons in $TlCuCl_3$ [10].

Certain magnetic insulators such as $TlCuCl_3$ consist of closely paired spin-$\frac{1}{2}$-particles, forming dimers with a spin-singlet ($S = 0$) ground state and triplet ($S = 1$) bosonic excitations called triplons (note that terms triplon and magnon are used interchangeably in most literature since they have the same quantum numbers). Thereby the singlet ground state is identified with the absence of a triplon and the excited triplet state with the presence of a triplon.
Considering $TlCuCl_3$, there exist several different interactions. The antiferromagnetic intradimer interaction J_0 is the strongest interaction. Furthermore there exist two relevant

interdimer interactions J_1 and J_2. The J_1-interaction is the coupling between neighbouring dimers of the same layer while the J_2-interaction is the coupling between dimers of different layers (see Fig. 1). If the interdimer interactions are weak, the ground state consists of non-magnetic singlets and remains without long-range magnetic order down to absolute zero temperature [7].

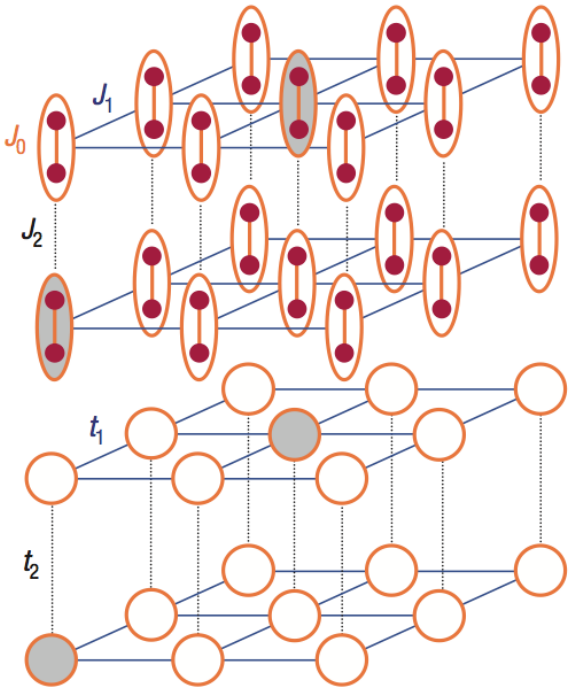

Figure 1: From [7]. Dimers of $TlCuCl_3$ with dominant antiferromagnetic intradimer interaction J_0 and interdimer interactions J_1 and J_2. Triplet states (grey, top) are mapped onto quasiparticle bosons (triplons, bottom).

The BEC transition occurs when the energy of one of the Zeeman split triplet excitations intersects the ground-state singlet, resulting in a long-range magnetic order. This can be achieved by applying a critical external magnetic field so that the Zeeman energy $g\mu_B\mu_0 H$ (where g is the Landé factor, μ_B is the Bohr magneton, μ_0 is the magnetic constant and H is the external magnetic field) overcomes this spin gap (see Fig. 2) [11].
The energy (up to the first order in J_1) of a triplon in a square lattice of dimers has the following form:

$$\epsilon(\vec{k}) = J_0 + J_1 \left[\cos\left(k_x a\right) + \cos\left(k_y a\right)\right] - g\mu_B\mu_0 H S^z, \tag{1}$$

where $\vec{k} = (k_x, k_y)$ is the wave vector of the triplon, a is the lattice constant and $S^z = 0, \pm 1$ is the spin projection of the triplon along the quantization axis.
The last term in Eq. (1) is the Zeeman term which controls the density of triplons. As a consequence of this, controlling the external magnetic field is equal to controlling the number of triplons appearing in the ground state. The magnetic field then acts as a chemical potential [13].
The first critical field H_{c1} defines the strength of the magnetic field where the excitation

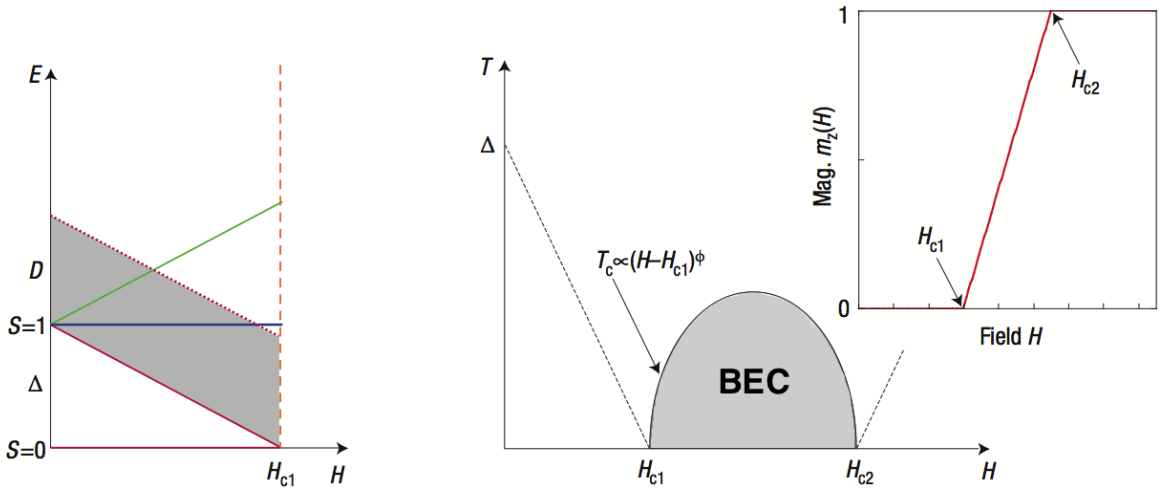

Figure 2: From [7], modified. Zeeman splitting of the triplet states with gap Δ and bandwidth D (left). Resulting phase diagram where a magnon BEC occurs. Close to H_{c1} and H_{c2} the phase boundary follows a power law $T_c \propto (H - H_{c1})^{\phi}$. Inset, magnetization curve $m_z(H)$ for a three-dimensional dimer spin system (right).

energy of the triplon with $S^z = -1$ crosses zero (see Fig. 2, left). The second critical field H_{c2} is reached when the magnetization saturates and each site is occupied by one triplon. The system's new ground state then is $S^z = -1$. Furthermore, it can be seen from Fig. 2 (right) that at zero temperature the magnetization $m_z(H)$ is zero and only singlets exist below H_{c1}. Between the two critical fields the magnetization increases with increasing field because more and more triplons appear in the ground state [7].

1.3 BEC phase of the spin-dimer systems $Ba_3Cr_2O_8$ and $Sr_3Cr_2O_8$

The detailed lattice structure of the isostructural $Ba_3Cr_2O_8$ and $Sr_3Cr_2O_8$ is shown in Fig. 3 (for detailed information on that topic see [15]). The focus lies on the phase diagrams of these two materials. Measurements to establish these phase diagrams were made by A. A. Aczel et al. (see Fig. 4 and Fig. 5). As one can see, the BEC phase of the $Ba_3Cr_2O_8$ can be found in lower magnetic fields (ranging from about 12.5 T to about 23.8 T) compared to $Sr_3Cr_2O_8$ (ranging from about 30.5 T to about 62.0 T). Furthermore, the maximum of the BEC phase of the Ba-compound can be found at temperatures of about 2.3 K whilst the maximum of the Sr-compound is at about 7.8 K [13, 14].

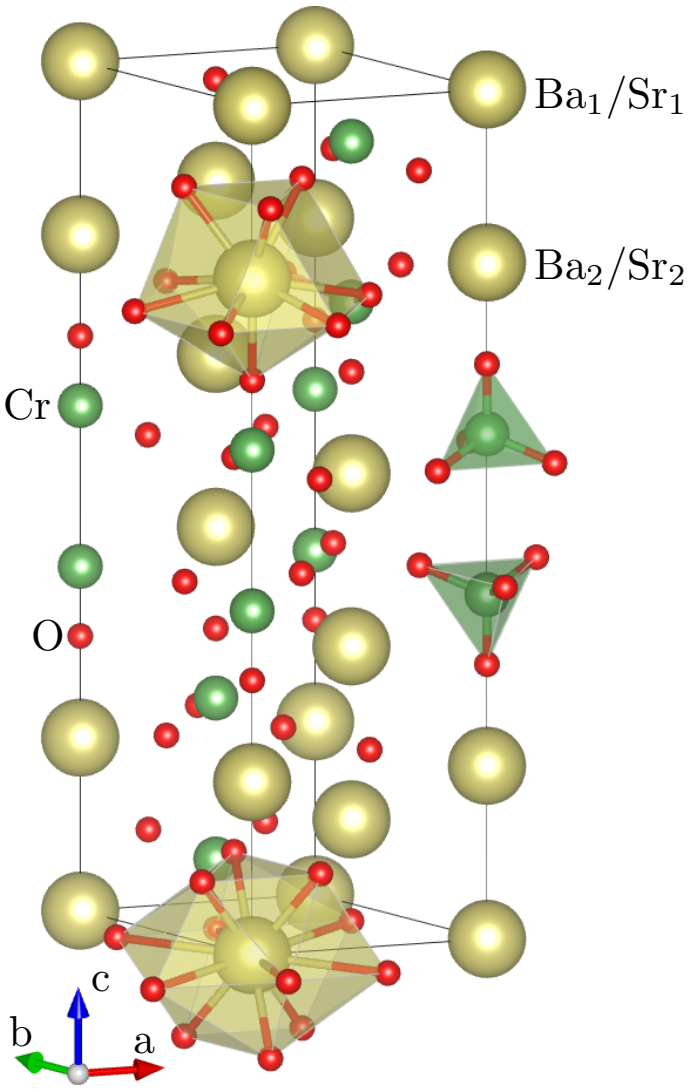

Figure 3: From [17], modified. Crystal structure of $Ba_{3-x}Sr_xCr_2O_8$ at room temperature. The Cr-tetrahedron is shown in dimer configuration on the right, the Ba_1/Sr_1-dodecatope is shown on the bottom and the Ba_2/Sr_2-decatope is shown on the top of the drawing.

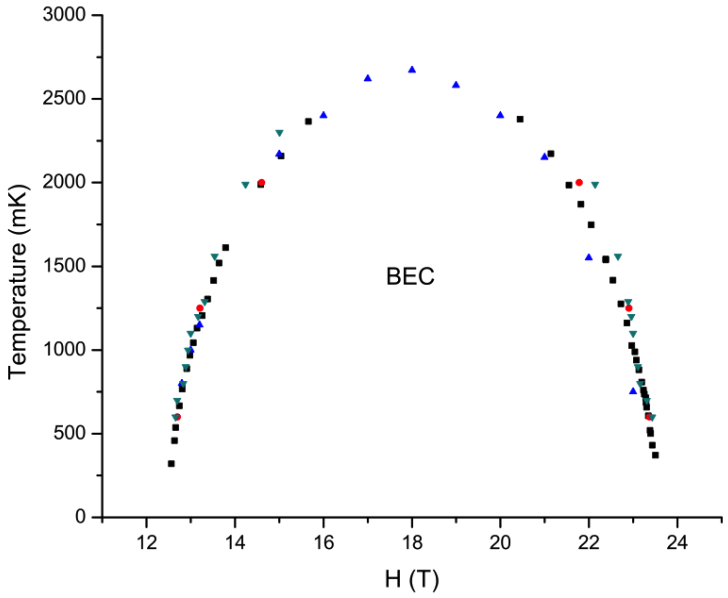

Figure 4: From [13], modified. Phase diagram of $Ba_3Cr_2O_8$.

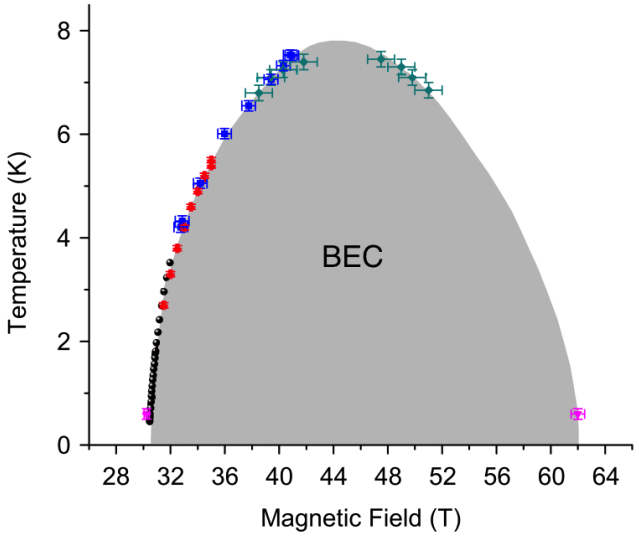

Figure 5: From [14], modified. Phase diagram of $Sr_3Cr_2O_8$. The ordered region is shaded as a guide to the eye.

2 Experimental Setup

2.1 Measuring *M(T)* in low magnetic fields

In order to measure the magnetic moment m as a function of the temperature T, the sample is moved inside a pick-up coil system. The equipment used for this work is the *QuantumDesign MPMS* (Magnetic Properties Measurement System) which consists of a superconducting quantum interference device (SQUID). The SQUID allows to measure the total magnetic moment with a high sensivity.
After weighing, the samples are put into a non-magnetic tube before being inserted into the MPMS. The sample space is then purged several times with He-gas to ensure a negigible oxygen content. Maintaining a low pressure He-atmosphere allows a sufficient thermal contact between the sample and the thermal bath of the MPMS.

The obtained magnetization data is analyzed by approximating the sample as a magnetic dipole and fitting the SQUID-signal accordingly. For the experiments, the main interest lies in the changes of the magnetization as a function of the temperature and not its absolute magnitude. Demagnetization factors are negligible in these systems [17].

2.2 Experimental setup of the high-field magnetometry measurements

The high-field magnetometry experiments were performed at the High Magnetic Field Laboratory in Dresden-Rossendorf (HZDR). In order to achieve extremely high magnetic fields, a capacitor with a stored electrical energy of about $E = 20$ MJ is discharged through a specifically designed coil (see Fig. 6). A quick discharge of the capacitor results in a high current in the coil, inducing fields up to $B_{\max} = 100$ T. From this rapidly changing field, a characteristic voltage pulse U_B is induced in the main pick-up coil.

In the same way does the changing magnetization of the sample induce a voltage U_M in the sample pick-up coil. An identical compensation coil is used to subtract the main field contribution. Due to the fact that the two pick-up coils do not produce exactly the same signals, a potentiometer is used to fine-tune the compensation.

The absolute field and magnetization as a function of time are found by integration of the voltage signals over time and applying a calibration factor. The features of the critical fields are calculated from the second derivative of the magnetization. The magnetic susceptibility is

$$\chi = \frac{\partial M}{\partial B} \propto \frac{U_M}{U_B}, \tag{2}$$

and from that, we obtain the second derivative of the magnetization as

$$\frac{\partial^2 M}{\partial B^2} = \frac{\partial \chi}{\partial B} = \frac{\Delta \chi}{\Delta B} = \frac{\Delta \chi}{U_B \Delta t} \propto \frac{\Delta \chi}{U_B} \tag{3}$$

where $\Delta\chi$ is the difference between consecutive values of χ and Δt is the (constant) time difference between consecutive measurements [17].

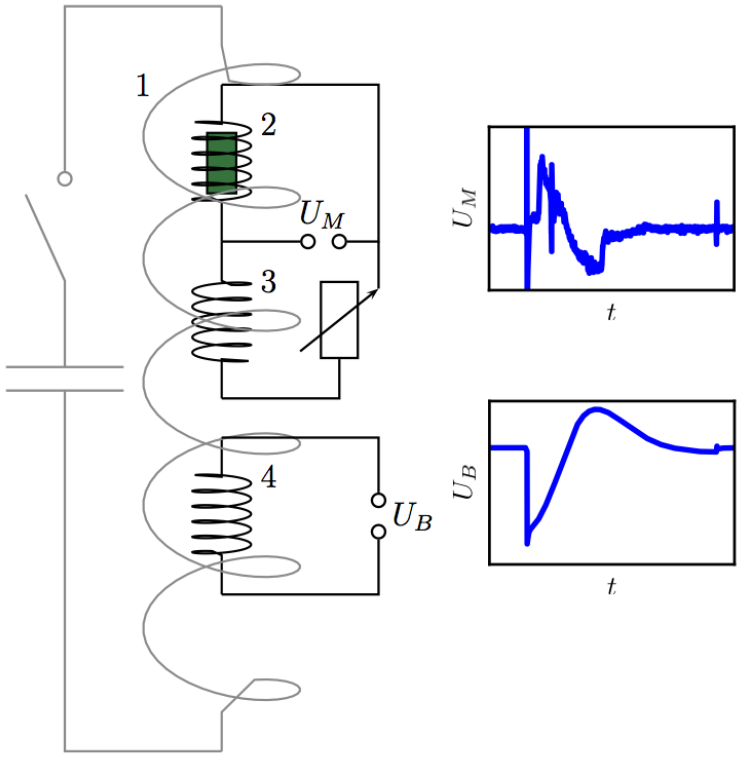

Figure 6: From [17]. Illustration of the principles of pulsed field magnetometry. 1: Main coil (with capacitor and switch), 2: Pick-up coil (with sample in green), 3: Compensation coil (with potentiometer), 4: Pick-up coil for main field. The plots on the right side show the voltages in the main pick-up coil (lower graph) and the sample pick-up coil (upper graph) as a function of time.

3 Measurements

3.1 Characterization of the samples

In order to test whether the samples exhibit the desired characteristics or not, the magnetic moment m as a function of the temperature T in a range from 2 K to 300 K was measured in a magnetic field of 1 T using the SQUID of the Physics Department of the University of Zurich. Fig. 7 shows the obtained data.

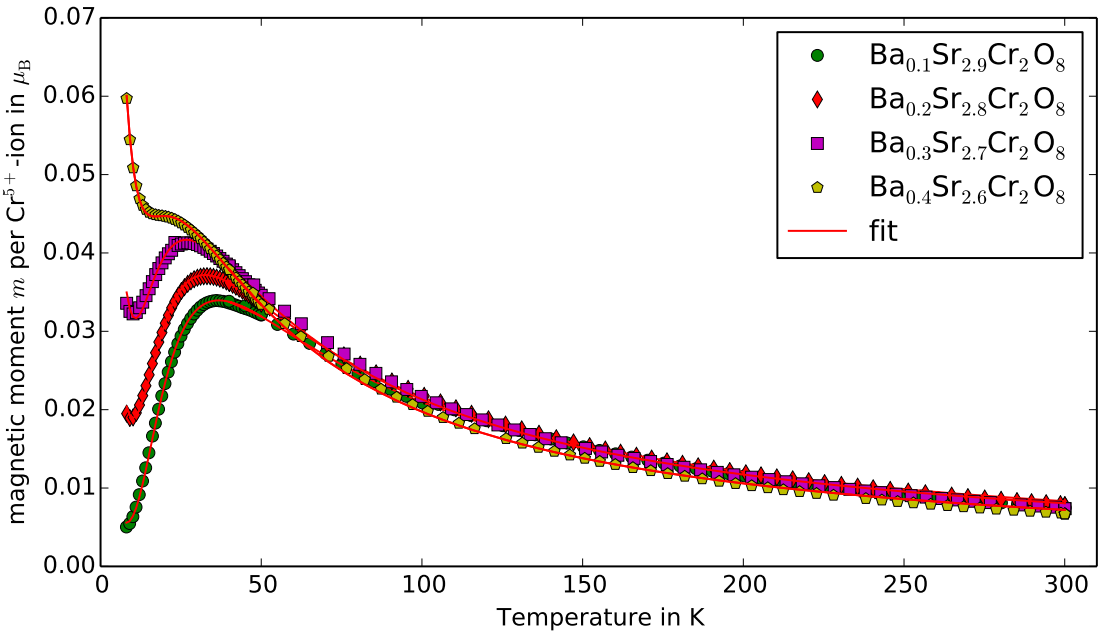

Figure 7: Measurement of the magnetic moment $m(T)$ per Cr^{5+}-ions in μ_B as a function of the temperature T for a magnetic field of 1 T for $Ba_{3-x}Sr_xCr_2O_8$. The red lines denote the fit according to the sum of Eqs. (4) and (5).

At temperatures above 70 K the thermal energy is large enough to overcome the dimer interaction between the Cr^{5+}-ions and $m(T)$ is similar to the case of a paramagnet. At temperatures below 70 K, however, the dimer interaction leads to the forming of paramagnetically disordered singlets.
The Bleaney-Bowers equation for interacting dimers is,

$$M(T) = \frac{n_d g^2 \mu_B \mu_0 H_{ext}}{J_e + k_B T \left(3 + e^{\frac{J_d}{k_B T}}\right)}, \tag{4}$$

where n_d is the density of the coupled ions, g is the Landé factor, μ_B is the Bohr magneton, μ_0 is the magnetic constant, H_{ext} is the external magnetic field, k_B is the Boltzmann constant, J_e is the interdimer interaction constant, J_d is the intradimer interaction constant and T is the temperature.

The paramagnetic background is based on the Brillouin function,

$$M(T) = n_P g \mu_B \frac{1}{2} \left(2 \coth \left(\frac{g \mu_B B_{\text{ext}}}{k_B T} \right) - \coth \left(\frac{g \mu_B B_{\text{ext}}}{2 k_B T} \right) \right), \tag{5}$$

where n_P is the density of the corresponding uncoupled ions. The data can be well described by the sum of Eq. (4) and Eq. (5).

3.2 High-field magnetometry

There are two different methods used to obtain the features of the critical magnetic fields of the high-field magnetometry experiments. The first method is to calculate the features from the first order derivative of M with respect to H. Fig. 8 shows the obtained data for values of x ranging from 2.5 to 3.0 (note that the data is smoothed using a gliding average). Conspicuous is the fact, that the saddle points for decreasing x get more and more smeared out.

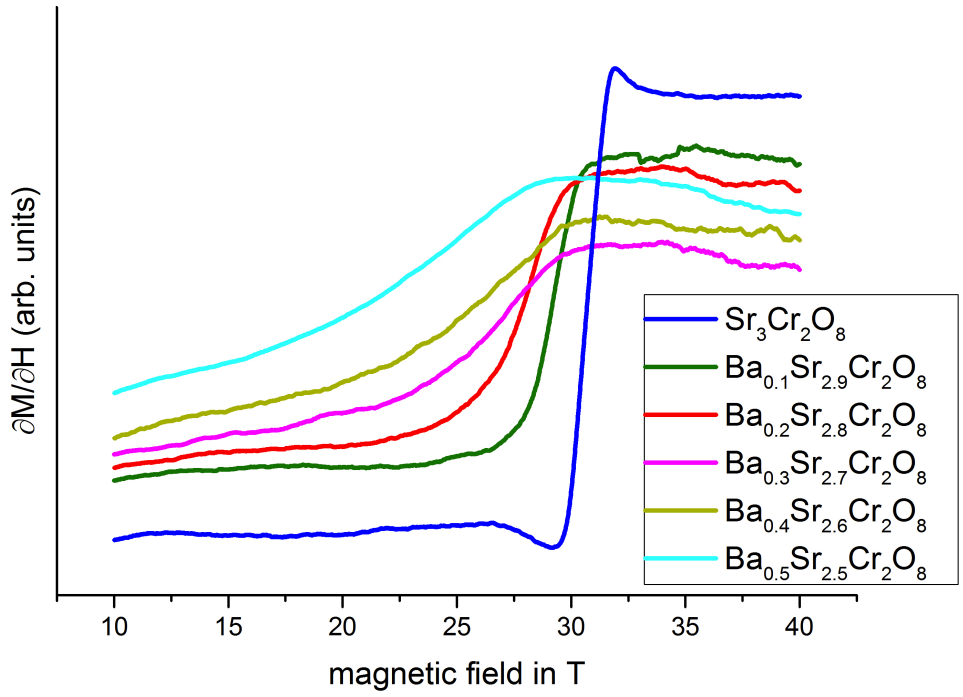

Figure 8: $\partial M/\partial H$ as a function of the external magnetic field H for $Ba_{3-x}Sr_xCr_2O_8$.

To obtain the features of the critical fields, the intersection points of linear fits are calculated as it is shown in Fig. 9 for the sample $Ba_{0.1}Sr_{2.9}Cr_2O_8$.
The intersection point is calculated by equalizing two straight lines $y = ax + b$ and $y = cx + d$,

$$x = \frac{d - b}{a - c}, \tag{6}$$

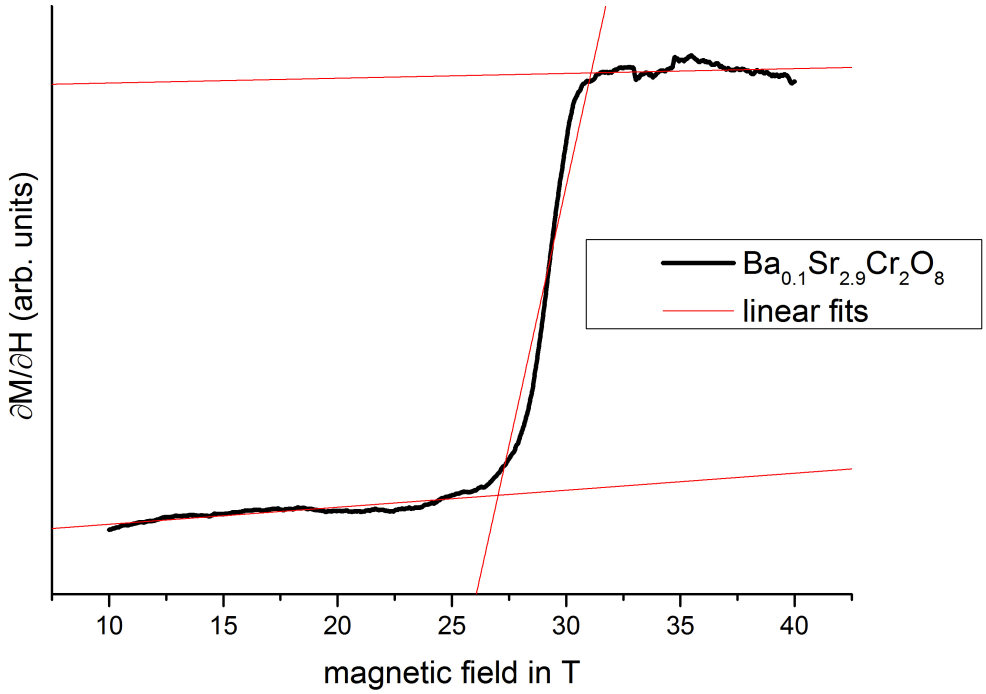

Figure 9: $\partial M/\partial H$ as a function of the magnetic field H for $Ba_{0.1}Sr_{2.9}Cr_2O_8$. The red lines represent linear fits which are used to obtain the features in the derivative of the magnetization.

and the error follows using simple error propagation

$$m_x = \sqrt{\left(\frac{1}{a-c}\right)^2 \cdot m_d^2 + \left(\frac{-1}{a-c}\right)^2 \cdot m_b^2 + \left(\frac{-(d-b)}{(a-c)^2}\right)^2 \cdot m_a^2 + \left(\frac{-(d-b)}{(a-c)^2}\right)^2 \cdot m_c^2}. \quad (7)$$

The plots and data analysis is made with *OriginPro 9.1* which automatically calculates all the fit-parameters and the corresponding errors (as can be seen in Tab. 1 for $Ba_{0.1}Sr_{2.9}Cr_2O_8$).

linear fit	intersection with y-axis	slope
1	$5.40(5) \cdot 10^{-6}$	$1.74(3) \cdot 10^{-7}$
2	$-2.76(3) \cdot 10^{-4}$	$1.06(1) \cdot 10^{-5}$
3	$5.17(3) \cdot 10^{-5}$	$4.9(9) \cdot 10^{-7}$

Table 1: Values for the parameters of the linear fits (calculated with *OriginPro 9.1*) for $Ba_{0.1}Sr_{2.9}Cr_2O_8$.

The results for the calculated features is summarized in Tab. 2. One sees that with decreasing x the features are shifted to lower magnetic fields.

material	feature 1	feature 2
$Sr_3Cr_2O_8$	29(7)	32(7)
$Ba_{0.1}Sr_{2.9}Cr_2O_8$	27(4)	31(5)
$Ba_{0.2}Sr_{2.8}Cr_2O_8$	25(3)	30(3)
$Ba_{0.3}Sr_{2.7}Cr_2O_8$	22(2)	31(2)
$Ba_{0.4}Sr_{2.6}Cr_2O_8$	22(2)	30(1)
$Ba_{0.5}Sr_{2.5}Cr_2O_8$	19(2)	29(2)

Table 2: Calculated features of the critical magnetic fields for the different materials.

The second method to determine the features of the critical fields is the analysis of the second order derivative of the magnetization M with respect to H. The BEC of triplons in spin-dimer systems is a second order phase transition. The system is described by the thermodynamic potential $G(T, H)$ (where G is the free enthalpy or Gibbs potential). From the Ehrenfest classification for phase transitions follows that a second order phase transition is characterized by a continuous first derivative of G with respect to its natural variables T and H at the transition point, whereas at least one of the second derivatives features a discontinuity at this point. This discontinuity then leads to a δ-peak in the third derivative of G.
The first derivative of G is the magnetization M, so that we have

$$M(T,H) = -\frac{\partial G}{\partial H} \tag{8}$$

$$\frac{\partial M}{\partial H} = -\frac{\partial^2 G}{\partial H^2} \tag{9}$$

$$\frac{\partial^2 M}{\partial H^2} = -\frac{\partial^3 G}{\partial H^3} \tag{10}$$

Fig. 10 shows the corresponding measurement. For decreasing x the features of the critical fields shift away from the reported critical field of $Sr_3Cr_2O_8$ (dashed line in Fig. 10) and are more and more smeared out, as it can be clearly seen for $Ba_{0.5}Sr_{2.5}Cr_2O_8$.

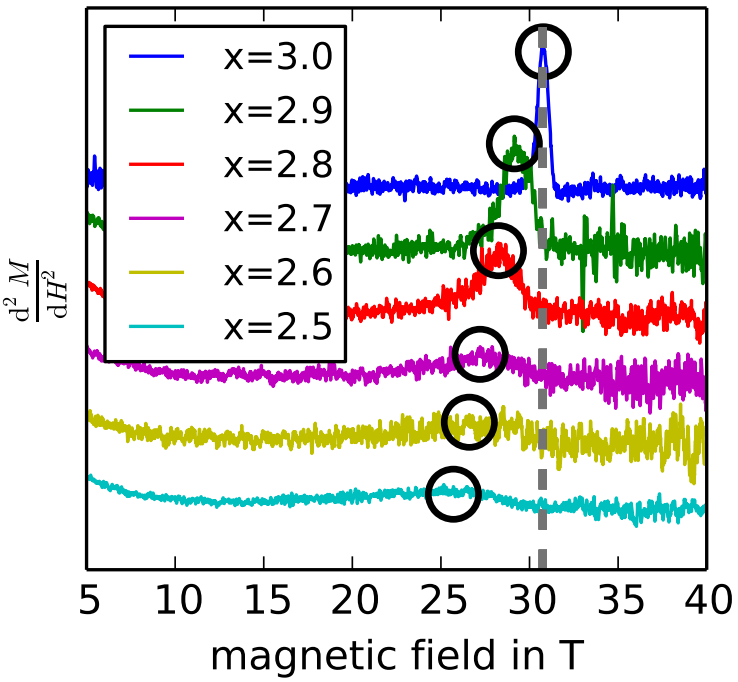

Figure 10: $\partial^2 M/\partial H^2$ as a function of the magnetic field H for $Ba_{3-x}Sr_xCr_2O_8$. The black circles mark the features due to the critical field. Note that the features are scaled differently for clarity. The dashed line marks the feature for a mono-crystal sample of $Sr_3Cr_2O_8$ [19].

4 Results and Discussion

The $Ba_{3-x}Sr_xCr_2O_8$ samples with values of x ranging from 2.5 to 3.0 have been measured in high-field magnetometry experiments. In order to calculate the critical magnetic field, two different methods have been used. The results calculated from these two methods can be seen in Fig. 11. For systems with weak interdimer interactions the minimal energy of a triplon does specifically depend on the intradimer interaction constant J_0 and the minimal energy should also correspond directly with the critical field. For a fixed value of g the critical field should thus be roughly proportional to J_0, if the interdimer interactions do not change [21]. Therefore, we can calculate an estimate for the critical field $H_c^e(x)$ in order to compare the results,

$$H_c^e(x) = H_c^{\mathrm{Sr_3}} \cdot \frac{J_0(x)}{J_0^{\mathrm{Sr_3}}}, \tag{11}$$

where $H_c^{\mathrm{Sr_3}}$ is the critical field for $Sr_3Cr_2O_8$ (calculated from Fig. 10), $J_0(x)$ is the intradimer interaction constant (calculated from Fig. 7) and $J_0^{\mathrm{Sr_3}}$ is the intradimer interaction constant of $Sr_3Cr_2O_8$.
Besides the values $x = 2.5$ and $x = 2.7$, the extrema calculated in $\frac{d^2M}{dH^2}$ fit best with the estimated fields. One has to emphasize that these estimates only depends on the intradimer interaction constants whilst the higher order interaction constants are neglected. Furthermore, from the $\frac{d^2M}{dH^2}$ data we can also conclude that the critical fields shift to lower magnetic fields for increasing x (see Fig. 10).
Beyond that, only the critical field H_{c1} could be observed in these measurements. The reason for that stems from the fact that only fields up to 60 T were applied.

For future experiments, I suggest to apply magnetic fields up to 65 T in order to measure the second critical field H_{c2} as well. Furthermore, from heat capacity measurements it would be possible to determine the full phase diagram for $Ba_{3-x}Sr_xCr_2O_8$ similar to Fig. 4 and Fig. 5.

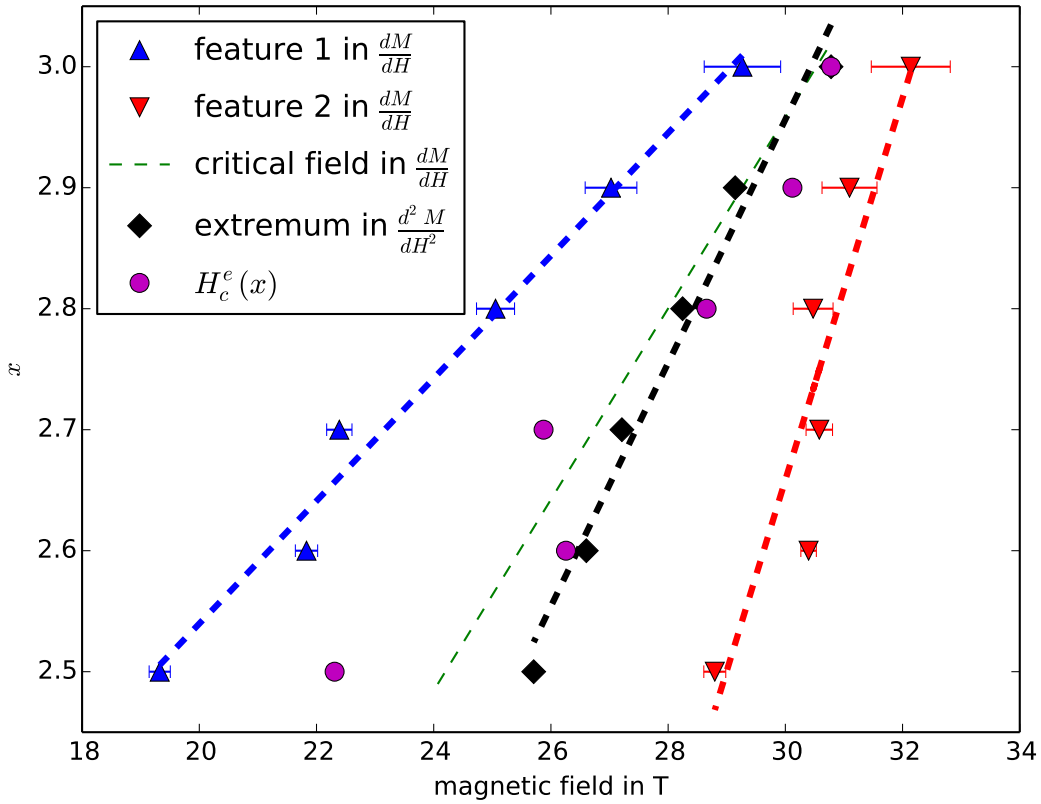

Figure 11: The red and blue triangles represent the features in dM/dH an the dashed green line represents the critical fields in dM/dH. The extrema calculated from d^2M/dH^2 are represented by the black diamonds. As a comparison, the estimated critical field $H_c^e(x)$ (Eq. (11)) is plotted (magenta circles), where the value for $x = 2.5$ is taken from [20]. The bold dashed lines represent trendlines as a guide to the eye.

5 References

[1] Townsend, C., Ketterle, W., Stringari, S. *Bose-Einstein condensation*. Physics World, March 1997.

[2] Einstein, A. *Quantentheorie des einatomigen idealen Gases - Zweite Abhandlung*. Berlin: Sitzungsberichte der Preussischen Akademie der Wissenschaften, 1925.

[3] Bose, S. N. *Plancks Gesetz und Lichtquantenhypothese*. Berlin: Zeitschrift für Physik 26, 1924.

[4] Annett, J. *Superconductivity, Superfluids und Condensates*. Oxford University Press, 2003.

[5] Griffin, A. *A brief History of our Understanding of BEC: from Bose to Beliaev*. Società Italiana de Fisica, 1999.

[6] Bloch, F. *Zur Theorie des Ferromagnetismus*. Zeitschrift für Physik 61, 206-219 (1930).

[7] Giamarchi, T., Rüegg, C., Tschernyshyov, O. *Bose-Einstein condensation in magnetic insulators*. Nature Publishing Group, 198-204 (2008).

[8] Kittel, C. *Einführung in die Festkörperphysik*. Munich: Oldenbourg, 2005.

[9] Matsubara, T., Matsuda, H. *A Lattice Model of Liquid Helium, I*. Progress of Theoretical Physics 16, 569-582 (1956).

[10] Nikuni, T., Oshikawa, M., Oosawa, A., Tanaka, H. *Bose-Einstein Condensation of Dilute Magnons in $TlCuCl_3$*. Physical Review Letters 84, 5868-5871 (2000).

[11] Rüegg, C., Cavadini, N., Furrer, A., Güdel, H.-U., Krämer, K., Mutka, H., Wildes, A., Habicht, K., Vorderwisch, P. *Bose-Einstein condensation of the triplet states in the magnetic insulator $TlCuCl_3$*. Nature 423, 62-65 (2003).

[12] Dodds, T., Yang, B. J., Kim, Y. B. *Theory of magnetic-field-induced Bose-Einstein condensation of triplons in $Ba_3Cr_2O_8$*. Physical Review B 81, 2010.

[13] Aczel, A. A., Kohama, Y., Jaime, M., Ninios, K., Chan, H. B., Balicas, L., Dabkowska, H. A., Luke, G. M. *Bose-Einstein condensation of triplons in $Ba_3Cr_2O_8$*. Physical Review B 79, 2009.

[14] Aczel, A. A., Kohama, Y., Marcenat, C., Weickert, F., Jaime, M., Ayala-Valenzuela, O. E., McDonald, R. D., Selesnic, S. D., Dabkowska, L., Luke, G. M. *Field-induced Bose-Einstein Condensation of Triplons up to 8 K in $Sr_3Cr_2O_8$*. Physical Review Letters 103, 2009.

[15] Ulrich, L. *Strukturelle und magnetische Eigenschaften des Spin-Dimer Systems $Ba_{3-x}Sr_xCr_2O_8$*. Bachelor Thesis at the University of Zurich, 2013. `http://www.physik.uzh.ch/groups/schilling/bama/BAUlrich.pdf`

[16] Clarke, J. *Principles and Applications of SQUIDs*. Proceedings of the IEEE Vol. 77, 1989.

[17] Grundmann, H. PhD-thesis, 2014.

[18] Nolting, W. *Grundkurs Theoretische Phyisk 6. Statistische Physik*. Berlin: Springer, 2007.

[19] Quintero-Castro, D. L., Lake, B. and Wheeler, E. M., Islam, A. T. M. N., Guidi, T., Rule, K. C., Izaola, Z., Russina, M., Kiefer, K., Skourski, Y. *Magnetic excitations of the gapped quantum spin dimer antiferromagnet* $Sr_3Cr_2O_8$. Physical Review Letters B 81, 014415 (2010).

[20] Grundmann, H., Schilling, A., Marjerrison, C. A., Dabkowska, H. A., Gaulin, B. D. *Structure and magnetic interaction in the solid solution* $Ba_{3-x}Sr_xCr_2O_8$. Mat. Res. Bull. 48, 3108-3111 (2013).

[21] Leuenberger, B., Stebler, A., Güdel, H. U., Furrer, A., Feile, R., Kjems, J. K. *Spin dynamics of an isotropic singlet-ground-state antiferromagnet with alternating strong and weak interactions. An inelastic-neutron-scattering study of the dimer compound* $Cs_3Cr_2Br_9$. Physical Review B 30, 6300 (1984).

6 Acknowledgement

At first, I would like to thank Prof. Dr. A. Schilling for giving me the opportunity to do my Bachelor's thesis at his research group. Furthermore, I would like to thank my supervisors Henrik Grundmann and Fabian von Rohr for their support, the numerous explanations and their great guidance throughout my work. I appreciated also the help of Stefan Siegrist of the University of Zurich who prepared all the samples in the laboratory. The measurements at the high-field Laboratory in Dresden-Rossendorf (HZDR) would not have been possible without the help of Dr. Tobias Förster. Thank you!

7 Appendix

7.1 Determination of the critical magnetic fields using linear fits

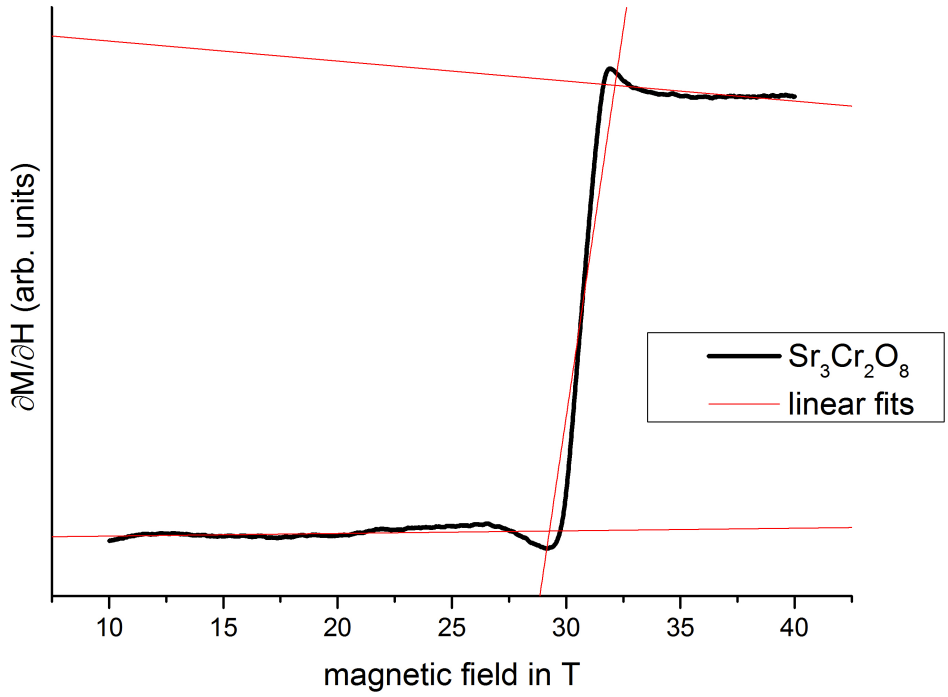

Figure 12: $\partial M/\partial H$ as a function of the magnetic field H for $Sr_3Cr_2O_8$. The red lines represent linear fits.

linear fit	intersection with y-axis	slope
1	$-1.71(7) \cdot 10^{-6}$	$3.8(4) \cdot 10^{-7}$
2	$-6.6(1) \cdot 10^{-3}$	$2.24(3) \cdot 10^{-5}$
3	$7.30(4) \cdot 10^{-5}$	$-2.9(1) \cdot 10^{-6}$

Table 3: Values for the parameters of the linear fits (calculated with *OriginPro 9.1*) for $Sr_3Cr_2O_8$.

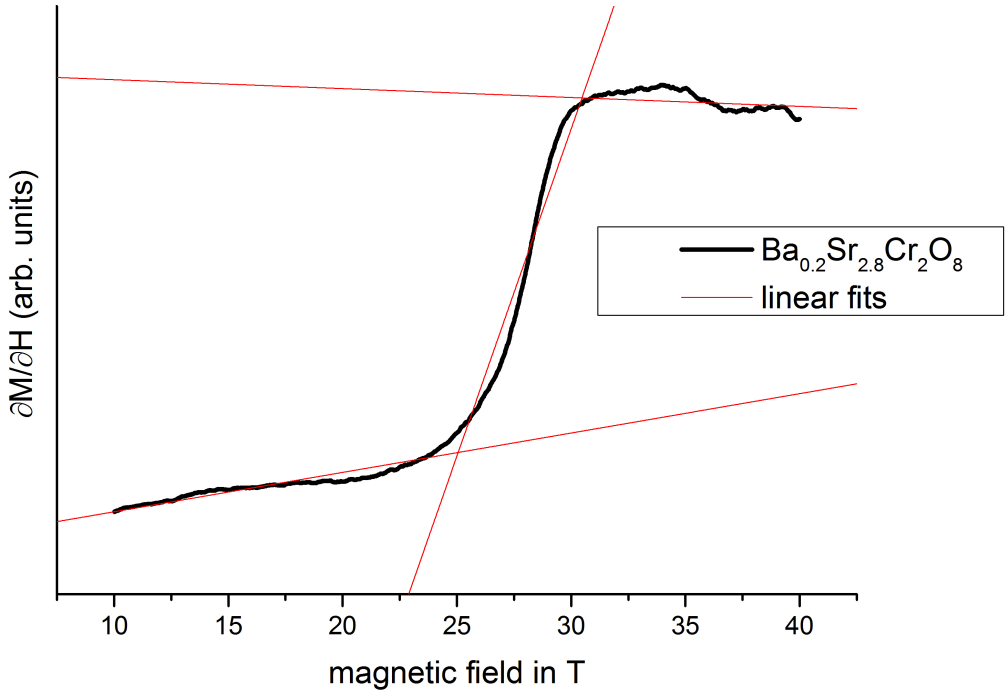

Figure 13: $\partial M/\partial H$ as a function of the magnetic field H for $Ba_{0.2}Sr_{2.8}Cr_2O_8$. The red lines represent linear fits.

linear fit	intersection with y-axis	slope
1	$4.40(9) \cdot 10^{-6}$	$4.02(5) \cdot 10^{-7}$
2	$-1.53(2) \cdot 10^{-4}$	$6.68(5) \cdot 10^{-6}$
3	$5.34(4) \cdot 10^{-5}$	$-9(1) \cdot 10^{-6}$

Table 4: Values for the parameters of the linear fits (calculated with *OriginPro 9.1*) for $Ba_{0.2}Sr_{2.8}Cr_2O_8$.

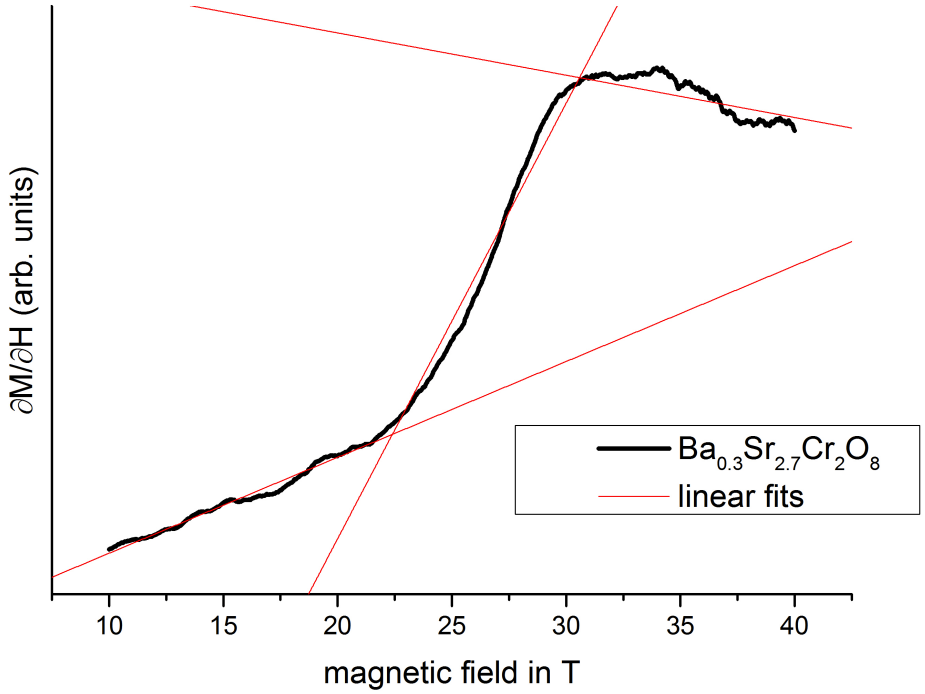

Figure 14: $\partial M/\partial H$ as a function of the magnetic field H for $Ba_{0.3}Sr_{2.7}Cr_2O_8$. The red lines represent linear fits.

linear fit	intersection with y-axis	slope
1	$4.00(4) \cdot 10^{-6}$	$6.11(2) \cdot 10^{-7}$
2	$-4.45(4) \cdot 10^{-5}$	$2.78(1) \cdot 10^{-6}$
3	$4.87(3) \cdot 10^{-5}$	$-2.70(9) \cdot 10^{-7}$

Table 5: Values for the parameters of the linear fits (calculated with *OriginPro 9.1*) for $Ba_{0.3}Sr_{2.7}Cr_2O_8$.

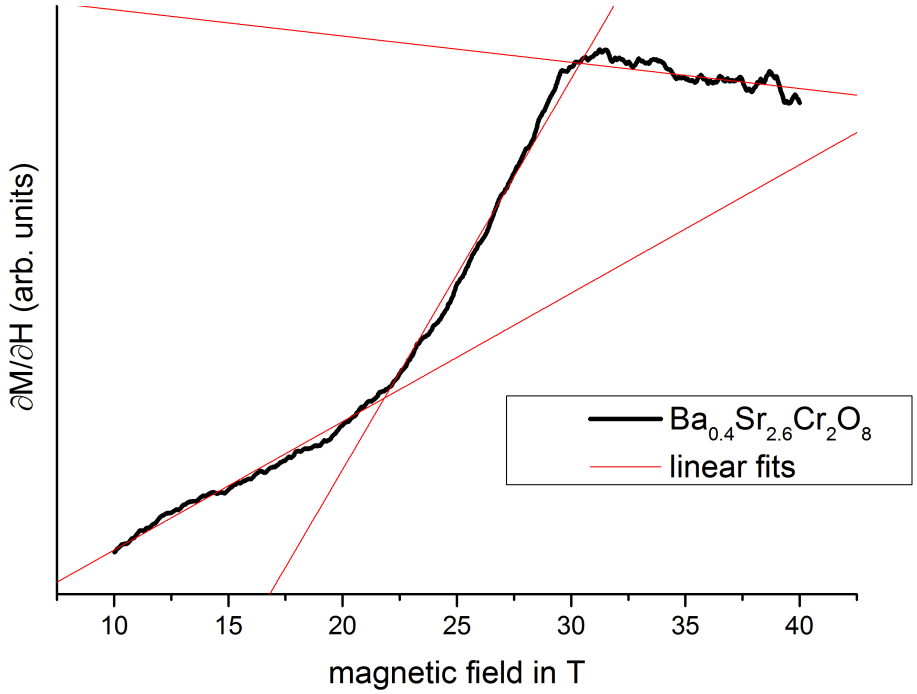

Figure 15: $\partial M/\partial H$ as a function of the magnetic field H for $Ba_{0.4}Sr_{2.6}Cr_2O_8$. The red lines represent linear fits.

linear fit	intersection with y-axis	slope
1	$4.63(6) \cdot 10^{-6}$	$8.19(4) \cdot 10^{-7}$
2	$-3.19(2) \cdot 10^{-5}$	$2.492(9) \cdot 10^{-7}$
3	$4.90(2) \cdot 10^{-5}$	$-1.68(7) \cdot 10^{-7}$

Table 6: Values for the parameters of the linear fits (calculated with *OriginPro 9.1*) for $Ba_{0.4}Sr_{2.6}Cr_2O_8$.

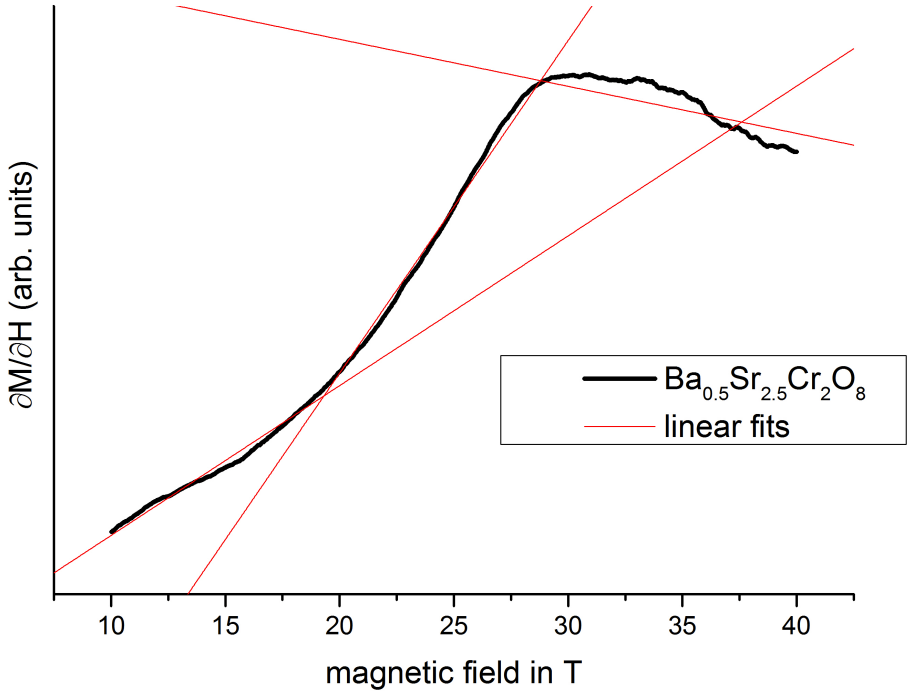

Figure 16: $\partial M/\partial H$ as a function of the magnetic field H for $Ba_{0.5}Sr_{2.5}Cr_2O_8$. The red lines represent linear fits.

linear fit	intersection with y-axis	slope
1	$8.81(8) \cdot 10^{-6}$	$1.019(5) \cdot 10^{-7}$
2	$-1.52(1) \cdot 10^{-5}$	$2.263(6) \cdot 10^{-7}$
3	$5.92(3) \cdot 10^{-5}$	$-3.20(10) \cdot 10^{-7}$

Table 7: Values for the parameters of the linear fits (calculated with *OriginPro 9.1*) for $Ba_{0.5}Sr_{2.5}Cr_2O_8$.